A&A 662, A20 (2022)
https://doi.org/10.1051/0004-6361/202243523

Astronomy & Astrophysics

Spectacular 240 kpc double-sided relativistic jets in a spiral-hosted narrow-line Seyfert 1 galaxy

A. Vietri[1], E. Järvelä[2], M. Berton[3], S. Ciroi[1], E. Congiu[4], S. Chen[5], and F. Di Mille[6]

[1] Dipartimento di Fisica e Astronomia "G. Galilei", Università di Padova, Vicolo dell'Osservatorio 3, 35122 Padova, Italy
e-mail: amelia.vietri@phd.unipd.it
[2] European Space Agency, European Space Astronomy Centre, C/Bajo el Castillo s/n, 28692 Villanueva de la Cañada, Madrid, Spain
[3] European Southern Observatory (ESO), Alonso de Córdova 3107, Casilla 19, Santiago 19001, Chile
[4] Departamento de Astronomía, Universidad de Chile, Camino del Observatorio 1515, Las Condes, Santiago, Chile
[5] Department of Physics, Technion 32000, Haifa 32000, Israel
[6] Las Campanas Observatory – Carnegie Institution for Science, Colina el Pino, Casilla 601, La Serena, Chile

Received 10 March 2022 / Accepted 29 March 2022

ABSTRACT

Narrow-line Seyfert 1 (NLS1) galaxies are a peculiar sub-class of active galactic nuclei (AGNe). They have demonstrated that the presence of relativistic jets in an AGN is not strictly related to its radio-loudness, the black hole mass, or their host galaxy type. Here, we present a remarkable example of a radio-quiet NLS1, 6dFGS gJ035432.8−134008 (J0354−1340). In our *Karl G. Jansky* Very Large Array observations at 5.5 GHz, the source shows a bright core with a flat spectral index and extended emission corresponding to very elongated jets. These are the largest double-sided radio jets found to date in an NLS1, with a de-projected linear size of almost 250 kpc. We also analysed near-infrared and optical images obtained by the *Magellan Baade* and the European Southern Observatory New Technology Telescope. By means of photometric decomposition and colour maps, we determined that J0354−1340 is hosted by a spiral or disc-like galaxy. Fully evolved relativistic jets have traditionally been associated with high-mass elliptical galaxies hosting the most massive black holes. Instead, our results confirm that powerful jets can also be launched and sustained by less massive black holes in spiral galaxies, implying that the launching of the jets is governed by factors other than those previously believed to be at play.

Key words. galaxies: groups: individual: 6dFGS gJ035432.8−134008 – galaxies: active – galaxies: Seyfert – galaxies: structure – infrared: galaxies

1. Introduction

Described for the first time by Osterbrock & Pogge (1985), narrow-line Seyfert 1 (NLS1) galaxies are a peculiar sub-class of active galactic nuclei (AGNe). Unlike broad-line Seyfert 1 galaxies (BLS1s), NLS1s are characterised by narrow permitted lines (Pogge 2011). By definition, they have a small full width at half maximum (FWHM) of (Hβ) lower than 2000 km s^{-1} (Goodrich 1989) and a flux ratio of [O III]λ5007/Hβ < 3 (Osterbrock & Pogge 1985). Unlike in Type 2 AGNe, the narrowness of the permitted lines is not related to obscuration. The low [O III]λ5007/Hβ < 3 ratio and the presence of strong Fe II multiplets in many NLS1s indicate an unobscured view of the broad-line region (BLR).

If the broadening of the permitted lines is due to Keplerian motion around a black hole (BH), their spectral features could be explained as a consequence of a low rotational velocity around a low-/intermediate-mass BH ($M_{\rm BH} < 10^8\,M_\odot$, Peterson 2011). Furthermore, considering that the bolometric luminosity, $L_{\rm bol}$, of these AGNe is comparable to that of BLS1s, it is inferred that a fraction of NLS1s accrete close to, or even above, the Eddington limit (Boroson & Green 1992). Some authors have, instead, proposed that the narrowness of the permitted lines in NLS1s is due to an inclination effect, caused by the lack of Doppler broadening, due to the pole-on view of a disc-like BLR (Decarli et al. 2008).

Whereas reverberation mapping has confirmed the low BH masses in some NLS1s (Peterson 2011), it is arduous and time-consuming to obtain reverberation data for large samples. Instead, their host galaxy morphologies can be used as a first-order estimate of the BH mass to investigate whether they actually are low. The host galaxy of an AGN interacts and co-evolves with the nuclear region, and thus the host galaxy morphology is linked to the properties of the central engine (Ferrarese & Merritt 2000; Morganti 2017). There are relations between the BH mass and properties of the bulge of its host galaxy (Magorrian et al. 1998), and, generally, more massive BHs are found to be hosted in elliptical galaxies, while spiral and disc galaxies tend to harbour less massive BHs (Salucci et al. 2000). As predicted by the low-mass scenario, it has been found that NLS1s, including the jetted ones, are preferably hosted by disc-like galaxies, often with pseudo-bulges and bars (Krongold et al. 2001; Crenshaw et al. 2003; Deo et al. 2006; Antón et al. 2008; Orban de Xivry et al. 2011; Mathur et al. 2012; Kotilainen et al. 2016; Olguín-Iglesias et al. 2017; D'Ammando et al. 2017, 2018; Järvelä et al. 2018; Berton et al. 2019; Hamilton et al. 2021). Due to this ensemble of properties, NLS1s are thought to be unevolved AGNe (Mathur et al. 2001).

Despite multiple observations suggesting that NLS1s have low-mass BHs, several NLS1s have been detected at γ-rays (Abdo et al. 2009a,b; Paliya et al. 2018; Foschini et al. 2021),

confirming the presence of powerful relativistic jets in them. This goes against the fact that, until recently, it was believed that powerful jets could only be harboured in elliptical galaxies, hosting the most massive supermassive BHs (Urry & Padovani 1995; Franceschini et al. 1998; Kotilainen et al. 2005). This result brings new evidence to support the idea that spiral galaxies with pseudo-bulges and low-mass BHs can launch and sustain powerful jets (Foschini 2011; Olguín-Iglesias et al. 2020). Mergers and interaction, which are more common in crowded regions, could play a role in triggering the launching of relativistic jets (Chiaberge et al. 2015). Jetted NLS1 galaxies residing in denser large-scale environments than non-jetted NLS1 galaxies support this scenario (Järvelä et al. 2017).

The presence of jets in NLS1s is not strictly related to their radio-loudness parameter R[1]. In only ≈7% of them the radio emission clearly dominates over the optical emission (Komossa et al. 2006), but even these sources do not necessarily harbour jets (Caccianiga et al. 2015). On the other hand, some NLS1s with no prior radio detections at any frequency have recently been detected at 37 GHz, confirming the presence of jets in them (Lähteenmäki et al. 2018; Berton et al. 2020; Järvelä et al. 2021).

The radio morphologies of NLS1s are diverse, and a fraction of them have been found to host large kiloparsec-scale jets (e.g., Berton et al. 2018; Järvelä et al. 2022). The most remarkable example may be the source we studied in this work, which shows very extended two-sided relativistic jets and was discovered by Chen et al. (2020). We studied this source in more detail by investigating its radio emission and the properties of its host galaxy. This paper is organised as follows. In Sect. 2 we describe the source, in Sect. 3 we present the radio analysis, Sect. 4 is dedicated to the near-infrared (NIR) and optical analyses of the host galaxy, and in Sect. 5 we discuss the results and give conclusions.

Throughout this study, we adopted a standard ΛCDM cosmology with a Hubble constant $H_0 = 67.8\,\mathrm{km\,s^{-1}\,Mpc^{-1}}$, considering a flat Universe with the matter density parameter $\Sigma_\mathrm{M} = 0.308$ and the vacuum density parameter $\Sigma_\mathrm{vac} = 0.692$ (Planck Collaboration XIII. 2016). For spectral indices, we adopted the convention of $S_\nu \propto \nu^\alpha$ at frequency ν.

2. 6dFGS gJ035432.8−134008

The target of this study is the NLS1 6dFGS gJ035432.8−134008 (hereafter J0354−1340, RA 03:54:32.85, Dec −13:40:07.24) at $z = 0.076$. This source was classified as an NLS1 by Chen et al. (2018) using a Six-degree Field Galaxy Survey spectrum. On the basis of the Hβ emission line dispersion and the continuum luminosity at 5100 Å, its BH mass is estimated to be $M_\mathrm{BH} \approx 9.8 \times 10^6\,M_\odot$. The radio morphology of J0354−1340 was studied by Chen et al. (2020), who classified this source as a Fanaroff–Riley II (FR II) radio galaxy (Fanaroff & Riley 1974). It has a compact central core, probably the jet-base, with a flat in-band spectral index. This NLS1 also shows considerable extended emission at both sides of the core at kiloparsec-scales. Chen et al. (2020) reported the projected extent of the southern radio emission to be 93.5 kpc and that of the northern to be 83.9 kpc; they measured the total integrated luminosity of $\nu L_{\nu,\mathrm{int}} \approx 3.8 \times 10^{39}\,\mathrm{erg\,s^{-1}}$ at 5.5 GHz. It should be noted that despite its unusual radio properties, the radio emission of J0354−1340 is not considerably brighter than its optical emission (Chen et al. 2020).

[1] Radio-loudness R is defined as the ratio between the radio 5 GHz flux density and the optical B-band flux density (Kellermann et al. 1989).

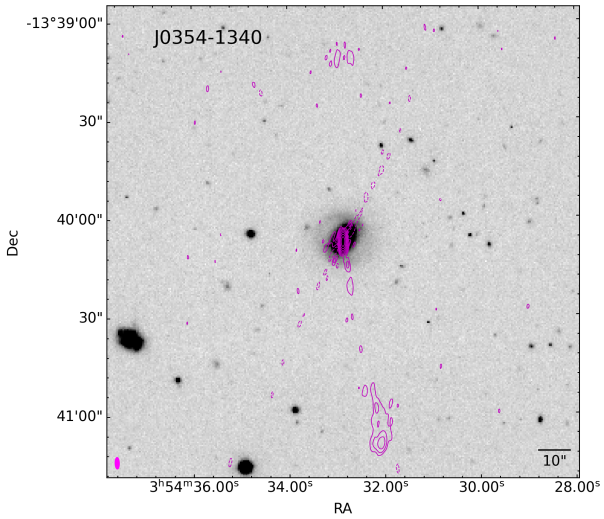

Fig. 1. Radio map of J0354−1340 overlaid with the J-band host galaxy image. The rms of the radio map is 8 μJy beam^{-1}. The relative contour levels are at rms × −3, 3 × 2^n $n \in [0, 7]$. The beam size is 5.25 kpc × 1.93 kpc.

3. Radio morphology

In this work, we used the same *Karl G. Jansky* Very Large Array (JVLA) data as Chen et al. (2020), but we performed a more detailed analysis. The radio data were obtained in February 2019 with the JVLA in C-configuration, centred at 5.5 GHz with a bandwidth of 2 GHz and divided into 16 spectral windows. The exposure time was 30 min and the angular resolution 3.5″, yielding a theoretical image sensitivity of ∼7 μJy beam^{-1}. The data were calibrated using the VLA pipeline version 5.4.0. For further data reduction and analyses we used Common Astronomy Software Applications (CASA) version 6.1.2-7. The data of J0354−1340 were split from the measurement set and averaged in time (10 s) and frequency (64 channels). To obtain the radio map, the tapered map, and the spectral index map, we used the multi-term multi-frequency synthesis (`mtmfs`) method implemented in CASA and followed the procedures by Wiegert et al. (2015) and Järvelä et al. (2022). The `mtmfs` algorithm models the wide-band sky-brightness distribution as a linear combination of spatial and spectral basis functions and performs image reconstruction (Rau & Cornwell 2011). The radio map, overlaid with the J-band host galaxy image (Fig. 1), shows extended emission corresponding to very elongated jets, which are located on the south-west and northern sides of the nucleus. We hypothesise the northern emission is real, albeit being detected only at 3σ, because the archival National Radio Astronomy Observatory VLA Sky Survey radio map shows extended emission toward north. Since J0354−1340 shows extended structures, we convolved the visibilities with a Gaussian taper with a FWHM of 15 $k\lambda$ to enhance the extended emission sensitivity. The tapered map, overlapped on the J-band image of the source, is shown in Fig. 2. However, the tapered map does not reveal new regions of radio emission. The spectral index map (Fig. 3) shows a flat core, as is typically seen in blazars. The spectral index of the lobe is approximately −0.5, which is slightly higher than the characteristic spectral index of −0.7 of optically thin synchrotron

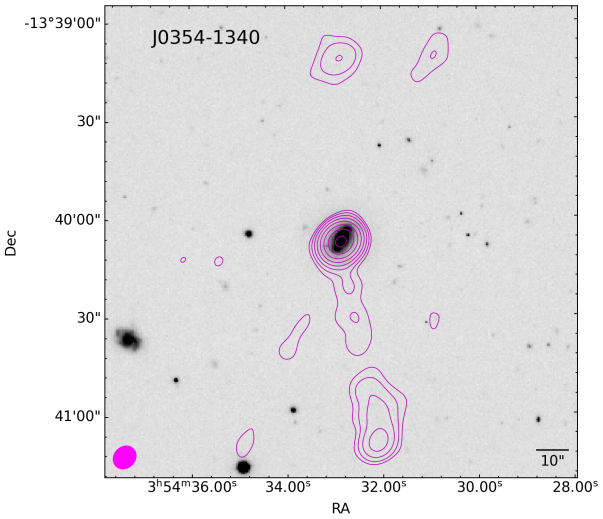

Fig. 2. Tapered map of J0354−1340 overlaid with the *J*-band host galaxy image. The relative contour levels are at rms × −3, 3 × 2^n $n \in [0, 7]$. The rms is 11 μJy beam^{-1}. The beam size is 11.10 kpc × 9.50 kpc.

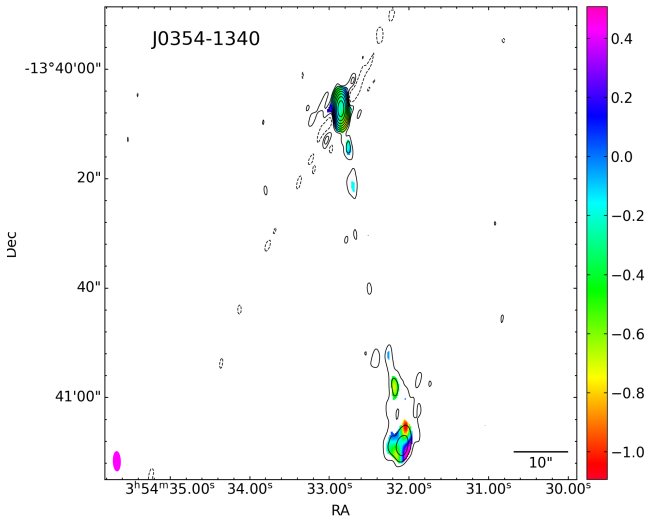

Fig. 3. Spectral index map of J0354−1340, showing only the core and the southern emission. The signal-to-noise ratio of the northern emission is too low to calculate its spectral index. The beam size is the same as in Fig. 1.

emission. CASA also provides the empirical error associated with the spectral indices, as shown in Fig. 4.

We measured the peak flux density and its error, produced by CASA, by fitting a 2D Gaussian to the core. We also measured the core and the extended emission flux densities within the 3σ contour. The errors related to the flux densities were estimated as the rms (∼8 μJy) multiplied by the square root of the area covered by the outermost contour expressed in units of beam (Berton et al. 2018). All the measurements with their respective errors are reported in Table 1.

Furthermore, we estimated the de-projected linear size, the orientation, and the age of the jet. We estimated the inclination using two different speeds for the jet: the somewhat unrealistic $v_{\rm jet} = 0.99\,c$, which gives an upper limit for the inclination, and a more realistic $v_{\rm jet} = 0.5\,c$ (e.g., Giroletti & Polatidis 2009). Since we were able to detect emission also from the receding jet, we can use the flux density ratio of the approaching (f_+) and the

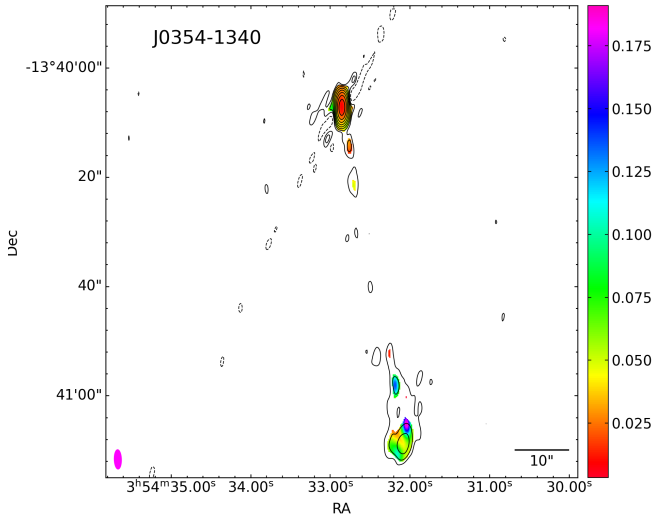

Fig. 4. Error spectral index map of J0354−1340.

Table 1. Radio properties of the source.

Region	Flux density
Core, peak	5.25 ± 0.02 mJy beam^{-1}
Core, total	4.88 ± 0.02 mJy
North, total	0.09 ± 0.01 mJy
South, total	0.76 ± 0.03 mJy
Total	5.73 ± 0.04 mJy

Notes. Columns: (1) Region; (2) Flux density.

receding jet (f_-) to estimate the inclination, θ, that is the angle with respect to the line of sight, using (Beckmann & Shrader 2012):

$$\frac{f_+}{f_-} = \left(\frac{1+\beta\cdot\cos(\theta)}{1-\beta\cdot\cos(\theta)}\right)^{(2-\alpha)}, \quad (1)$$

where α is the spectral index of the jet set to −1. We chose the standard value of α since no reliable estimate was derived from the spectral index map. The flux densities were $f_+ = 0.76$ mJy and $f_- = 0.09$ mJy for the approaching and the receding jets, respectively. Assuming $\beta = 0.99$, Eq. (1) gives an estimate of the jet inclination of $\theta_1 = 70°$. This value represents an upper limit for the inclination of the jet. Using $\beta = 0.5$ instead, we obtained a more reasonable estimate of the jet inclination of $\theta_2 = 47°$.

We estimated the de-projected sizes of the jets using the more reasonable assumption of $\beta = 0.5$ and obtained $D^+_{\rm jet} = 127$ kpc and $D^-_{\rm jet} = 114$ kpc, giving a total extent of 241 kpc. Interestingly, they do not seem to be exactly aligned, but at an angle of 169°.

Finally, we estimated the age of the approaching jet as the ratio between its de-projected liner size and jet velocity. For $\beta = 0.99\,c$, the age is $t \sim 0.3$ Ma, while for $\beta = 0.5$, we have $t \sim 0.8$ Ma.

4. Host galaxy

4.1. Photometric decomposition

The NIR observations of J0354−1340 were carried out in October 2019 with the *Magellan Baade* 6.5 m telescope.

Table 2. Best fit parameters of J0354−1340 with $\chi^2_\nu = 1.27^{+0.09}_{-0.01}$.

Function	Mag	r_e (kpc)	n	Axial ratio	PA (°)	Notes
PSF	$14.29^{+0.39}_{-0.42}$					Nucleus
S1	$14.06^{+0.40}_{-0.55}$	$1.15^{+0.12}_{-0.75}$	$4.24^{+0.74}_{-2.03}$	$0.91^{+0.00}_{-0.00}$	$-45.81^{+0.56}_{-5.41}$	Bulge
S2	$13.72^{+0.42}_{-0.40}$	$8.63^{+0.79}_{-2.89}$	$0.56^{+0.08}_{-2.01}$	$0.83^{+0.04}_{-0.07}$	$-38.94^{+1.69}_{-0.0.}$	Disc
S3	$14.51^{+0.39}_{-0.60}$	$4.40^{+0.08}_{-0.33}$	$0.37^{+0.01}_{-0.12}$	$0.33^{+0.01}_{-0.06}$	$-28.24^{+0.02}_{-0.89}$	Bar

Notes. Columns: (1) function used in the model; (2) magnitude of the component in Ks-band; (3) effective radius; (4) Sérsic index; (5) axial ratio; (6) position angle; (7) physical interpretation.

The J- and Ks-band observations were performed using the wide-area NIR camera FourStar. During the observing night, the sky was clear and the seeing was approximately 0.5″ in both bands. The total exposure time was ≈1200 s and ≈760 s, for the $J-$ and Ks-band images, respectively. Standard reduction, photometric and astrometric calibrations, and sky subtraction were applied to the images with the Image Reduction and Analysis Facility (IRAF) Software. We performed a photometric decomposition of the Ks-band image using the 2D fitting algorithm GALFIT version 3.0.5 (Peng et al. 2010). More details about the photometric decomposition and host modelling are given in Appendix A.1. Since the AGN emission affects the host model, it needs to be modelled simultaneously with the galaxy. Because the AGN is a point-like source, this can be done by fitting it with a modelled point-spread function (PSF). We tried different approaches to create the PSF, and after several attempts the best model was obtained by fitting a nearby star with five Sérsic functions.

We modelled the host galaxy varying at each step the initial fitting parameters to make sure that the resulting model parameters were stable, and we also varied the number of components until the best, most stable fit was achieved. The variation of the sky background is the largest source of error in the fit. We estimated the σ_{sky} by measuring the standard deviation of the sky in several empty regions in the image and taking the average of those. There are three sources of error for the magnitude: the error related to the zero point calculation, the error reported for the star magnitude values in the 2MASS Catalogue[2], and the error we obtained from GALFIT by modelling the source with the $\pm\sigma_{sky}$ values. To obtain the total error, we summed the different sources of error in quadrature after converting to linear units. To estimate the errors of the other parameters, except the magnitude, we fitted the source with the $\pm\sigma_{sky}$ and used the difference between the resulting values and the best-fit values as the error. The best fit was achieved with four components: a PSF for the AGN and three Sérsic functions for the bulge (S1), for the disc (S2), and for the bar (S3). The goodness of fit was determined based on the χ^2_ν value, 1.27, and the fact that the output parameters remained physically reasonable and stable during the fit. The S1 component represents the bulge. However, likely due to the remarkable strength of the bar component and the bulge being only marginally resolved, our measurements of the Sérsic index of the bulge have a relatively high error (see Table 2). Therefore, we do not discuss its properties in the following, because the uncertainty is too high. New, higher resolution observations are needed to accurately measure its physical properties. S2 with $r_e = 8.63$ kpc, $n = 0.56$, and an axial ratio = 0.83 resembles a disc. The S3 is a bar-like component with $r_e = 4.40$ kpc, $n = 0.37$, and an axial ratio = 0.33.

[2] https://irsa.ipac.caltech.edu/Missions/2mass.html

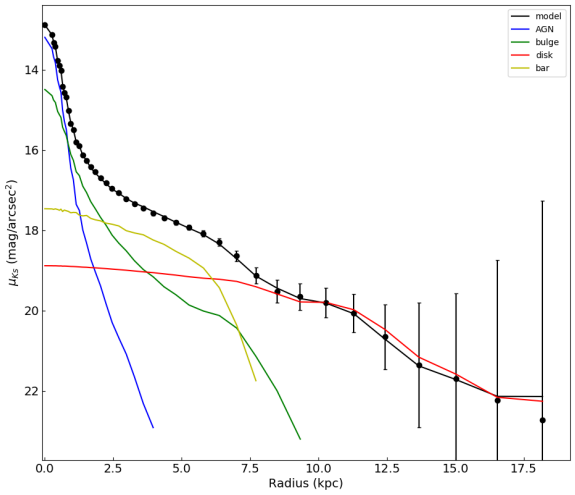

Fig. 5. Radial surface brightness profile of the galaxy. The image shows the model in black, the AGN component in blue, the bugle component in dark green, the disc component in red, and the bar component in light green.

We discovered that this NLS1 is hosted in a barred spiral or disc-like galaxy, while no further details can be given about the characterisation of the bulge, since it is not properly resolved. In the observed image, shown in the left panel of Fig. 6, it is possible to see the clear barred spiral shape, with a peculiar bar enhanced at the poles and a faint ring surrounding the whole galaxy. This galaxy shows a very complex structure, but since we are mainly interested in the main components of the galaxy we did not try to model the more complex features, such as the faint ring. The image also shows some small unmodelled regions outside the galaxy that also affect the χ^2_ν value, which is calculated for the whole fitting region. The model is shown in the central panel of Fig. 6. The residuals in the right panel of Fig. 6 show a ring-like structure around the centre, especially enhanced at the 'poles' of the bar, while in the centre there are both over- and under-subtracted regions. The radial surface brightness profile of the galaxy and the galfit components, obtained with *ELLIPSE* in IRAF, is shown in Fig. 5. The model matches the galaxy profile well; however, the disc component is unusually faint.

4.2. Colour images

The optical images of this source were obtained with the New Technology Telescope (NTT; proposal ID: NTT/106.21HS, PI M. Berton) in January 2021. The g- and i-band observations were performed using the ESO Faint Object Spectrograph and Camera version 2. The seeing was about 1.13″ for g and 1.08″ for the

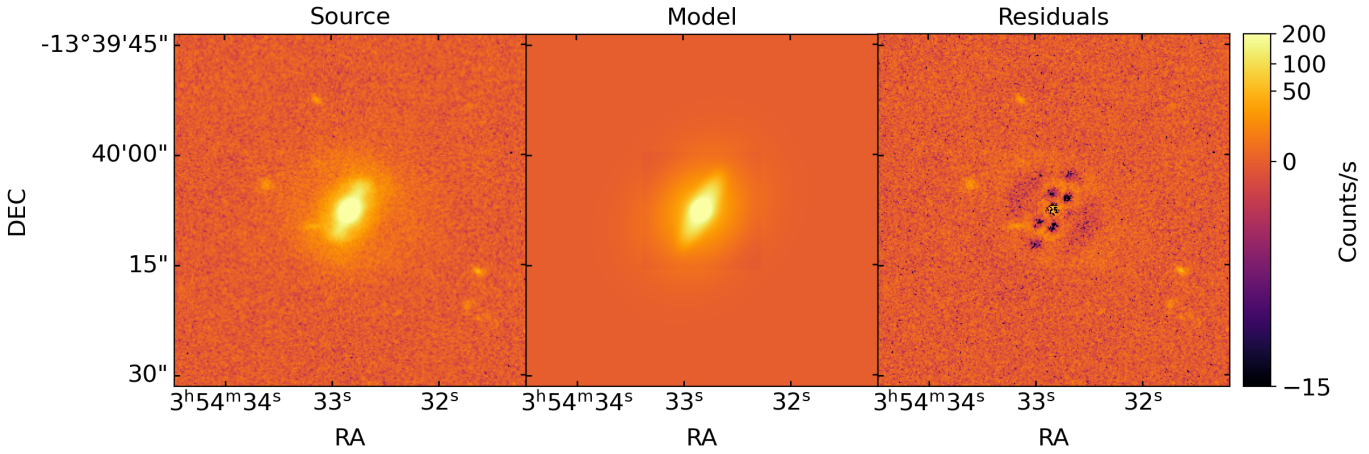

Fig. 6. GALFIT output images. *Left panel*: observed image in Ks band. The size of the image (that of the fitting region) is 47.7 arcsec, corresponding to 70.9 kpc. *Central panel*: model image of the galaxy. *Right panel*: residual image, smoothed over 2 px.

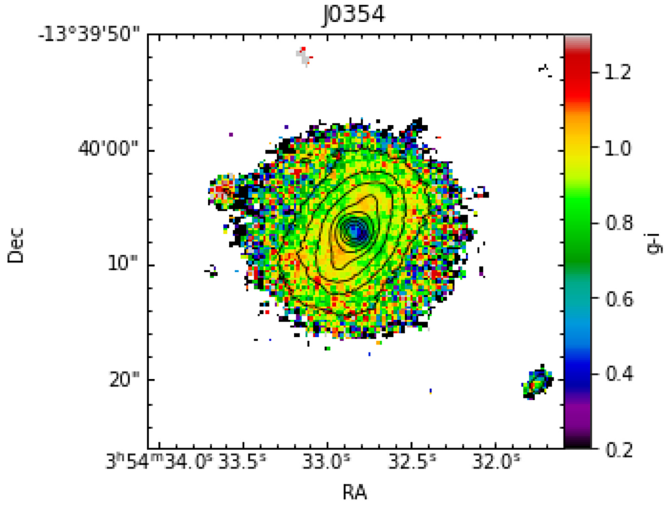

Fig. 7. $g - i$ colour map of J0354−1340.

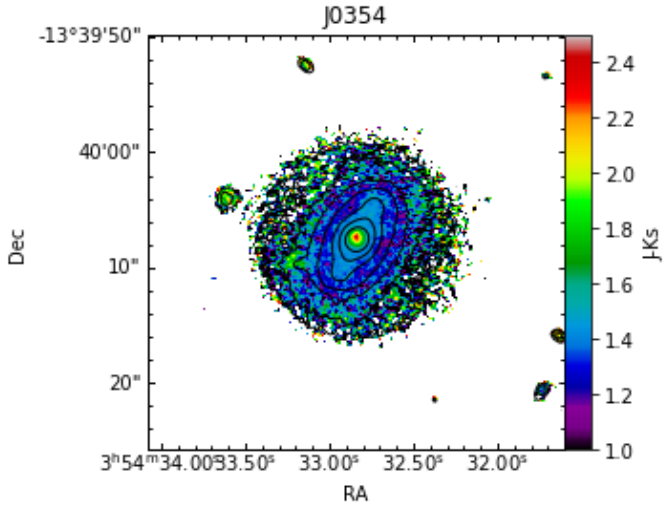

Fig. 8. $J - Ks$ colour map of J0354−1340.

i band, while the exposure time is 300 s for both images. We performed a standard reduction using IRAF, with bias and flat-field correction, followed by the alignment, sky subtraction, fringing removal, and combination of the images in each filter.

The $g - i$ colour map is shown in Fig. 7. The colour is quite uniform throughout the whole galaxy, except for the nucleus. The central region of the map is blue, showing $g - i \approx 0.4$, a value typically observed in green quasars (Klindt et al. 2019).

We also derived the $J - Ks$ colour map (Fig. 8). The colour is quite homogeneous and it is mainly blue; The difference between J and Ks magnitudes is ∼1.5, as would be expected for a Seyfert-like galaxy (Jarrett 2000). The central region's colour, corresponding to the AGN, is instead red, possibly due to dust extinction or old stars. As seen on the map, the bar is really prominent, possibly due to its abundant dust content. In the NIR, the stellar populations can also contribute to the colour; old stars especially may make the colour redder.

5. Discussion

In radio, J0354−1340 shows a bright compact core and extended emission, located to the southwest and on the north side of the central region (Fig. 1). These extended structures correspond to the radio lobe of the approaching and the receding jet, respectively. The presence of very extended jets in a source where the radio emission does not dominate over the optical emission is more proof that simple parameters, such as the radio-loudness, are ambiguous and should not be trusted or used (Järvelä et al. 2017; Padovani 2017; Lähteenmäki et al. 2018; Berton & Järvelä 2021). What makes this source truly peculiar among NLS1s and other AGNe with low BH masses is the size of the extended emission. The projected linear size of 100 kpc of each jet is consistent with those of FR II radio galaxies (Hardcastle et al. 1998; Kharb et al. 2008). J0354−1340 indeed harbours the largest radio jets in projected size found to date in an NLS1, whose projected jet sizes are usually of the order of a few kiloparsecs (Doi et al. 2012; Richards & Lister 2015; Congiu et al. 2017; Rakshit et al. 2018; Gabányi et al. 2018; Järvelä et al. 2022).

The largest estimated de-projected size of the jets among NLS1s is ∼1 Mpc in PMN J0948+0022 (Doi et al. 2019). However, this estimate is based on an assumption of a very low inclination, as the counter-jet is not visible in radio maps. Instead, J0354−1340 has the largest de-projected linear size ever

observed in an NLS1s, ∼240 kpc, with its viewing angle estimated from the jet/counter-jet flux density ratio. Naturally, our estimate also includes uncertainty due to the unknown jet speed and spectral index. The inclination derived from $v \sim c$, $\theta_1 = 70°$, is higher than typical values for type 1 AGNe (Peterson 1997). Therefore, the approximation $v_{\rm jet} = 0.99\,c$ is most probably not realistic in this case. The more reasonable approximation of $\beta = 0.5$ gives an inclination of $\theta_2 = 47°$, which is consistent with the range of viewing angles for type 1 AGNe. This value does not imply a face-on view of the nucleus and, for this reason, the BH mass should not be underestimated due to an inclination effect (Vietri et al. 2018). However, were the jet speed lower, it would also imply lower inclination, but it probably could not have resulted in the radio morphology we see in this source. Assuming a viewing angle of 47°, the de-projected size of the whole extended emission is ∼241 kpc. The extent of the jets in J0354−1340 is extraordinary and unprecedented among NLS1s, which usually harbour jets that are some hundreds of parsec to a few kiloparsecs long. The jets are huge compared to the host galaxy whose half-light radius we estimated to be ∼8.6 kpc, and extent beyond the host galaxy, reaching the intergalactic medium (IGM). The age of the approaching jet estimated using the reasonable approximation of $\beta = 0.5$ gives a lower limit of $\approx 8 \times 10^5$ years. This lies at the low tail of the age range of 10^5–10^7 years found for other jetted NLS1s (Czerny et al. 2009). The jets are not aligned and have an angle of 169° between them. We speculate that this is due to a combination of the motion of the galaxy through the IGM and the ram pressure induced by the IGM (Plewa et al. 1997; Savolainen et al. 2006).

Considering the spectral index map, the compact core, which probably represents the jet base, shows a flat in-band spectral index, as seen in blazars (Foschini et al. 2015). The spectral index of the extended emission, ≈−0.5, is slightly higher than the usual spectral index of ≈−0.7 of optically thin synchrotron emission. This may be due to interaction between the lobe and the IGM, which re-accelerates the electrons in the lobe and thus makes the spectral index flatter (Best et al. 1997).

The photometric decomposition of J0354−1340 shows that it is hosted in a barred spiral galaxy. The BH mass of this source is within the typical range for NLS1 (Peterson 2011), as mentioned in Sect. 2. This value is also consistent with the high end of the BH masses hosted in late-type spirals (Salucci et al. 2000). This further confirms that fully developed relativistic jets can be harboured in spirals, as proved by several authors (Keel et al. 2006; Mao et al. 2018; Järvelä et al. 2018; Olguín-Iglesias et al. 2020). Traditionally, the most powerful relativistic jets have been associated with the highly evolved massive elliptical galaxies with considerably higher BH masses, formed in dense large-scale environments. These galaxies undergo the phase of the formation of jets, that coincides with the formation of the classical bulge, probably induced by mergers (Kormendy & Gebhardt 2001; Urry 2003). In spiral galaxies, secular processes rather than interaction and mergers dominate the bulge growth, the BH activity, and the formation of pseudo-bulges (Costantin et al. 2022). Nevertheless, spiral galaxies have been found to host kiloparsec- or even megaparsec-scale relativistic jets (Hota et al. 2011). J0354−1340 fits this scenario, harbouring one of the largest radio jets found to date in an NLS1 that is hosted in a disc galaxy.

Acknowledgements. This paper includes data gathered with the 6.5 m *Magellan* Telescopes located at Las Campanas Observatory, Chile. Based on observations made with ESO Telescopes at the La Silla Paranal Observatory under ESO programme P106.21HS. M.B. and S.C. acknowledge the financial support from the visitor and mobility program of the Finnish Centre for Astronomy with ESO (FINCA), funded by the Academy of Finland grant No. 306531. M.B. is an ESO fellow. E.J. is a current ESA science fellow. E.C. acknowledges support from ANID project Basal AFB-170002.

References

Abdo, A. A., Ackermann, M., Ajello, M., et al. 2009a, ApJ, 699, 976
Abdo, A. A., Ackermann, M., Ajello, M., et al. 2009b, ApJ, 707, 727
Antón, S., Browne, I. W. A., & Marchã, M. J. 2008, A&A, 490, 583
Beckmann, V., & Shrader, C. R. 2012, Active Galactic Nuclei (Weinheim: Wiley-VCH Verlag GmbH)
Berton, M., & Järvelä, E. 2021, Astron. Nachr., 342, 1066
Berton, M., Congiu, E., Järvelä, E., et al. 2018, A&A, 614, A87
Berton, M., Congiu, E., Ciroi, S., et al. 2019, AJ, 157, 48
Berton, M., Björklund, I., Lähteenmäki, A., et al. 2020, Contrib. Astron. Obs. Skalnate Pleso, 50, 270
Best, P. N., Longair, M. S., & Rottgering, H. J. A. 1997, MNRAS, 286, 785
Boroson, T. A., & Green, R. F. 1992, ApJS, 80, 109
Caccianiga, A., Antón, S., Ballo, L., et al. 2015, MNRAS, 451, 1795
Chen, S., Berton, M., La Mura, G., et al. 2018, A&A, 615, A167
Chen, S., Järvelä, E., Crepaldi, L., et al. 2020, MNRAS, 498, 1278
Chiaberge, M., Gilli, R., Lotz, J. M., & Norman, C. 2015, ApJ, 806, 147
Congiu, E., Berton, M., Giroletti, M., et al. 2017, A&A, 603, A32
Costantin, L., Pérez-González, P. G., Méndez-Abreu, J., et al. 2022, ApJ, 929, 121
Crenshaw, D. M., Kraemer, S. B., & Gabel, J. R. 2003, AJ, 126, 1690
Czerny, B., Siemiginowska, A., Janiuk, A., Nikiel-Wroczyński, B., & Stawarz, Ł. 2009, ApJ, 698, 840
D'Ammando, F., Acosta-Pulido, J. A., Capetti, A., et al. 2017, MNRAS, 469, L11
D'Ammando, F., Acosta-Pulido, J. A., Capetti, A., et al. 2018, MNRAS, 478, L66
Decarli, R., Dotti, M., Fontana, M., & Haardt, F. 2008, MNRAS, 386, L15
Deo, R. P., Crenshaw, D. M., & Kraemer, S. B. 2006, AJ, 132, 321
Doi, A., Nagira, H., Kawakatu, N., et al. 2012, ApJ, 760, 41
Doi, A., Nakahara, S., Nakamura, M., et al. 2019, MNRAS, 487, 640
Fanaroff, B. L., & Riley, J. M. 1974, MNRAS, 167, 31P
Ferrarese, L., & Merritt, D. 2000, ApJ, 539, L9
Foschini, L. 2011, in Narrow-Line Seyfert 1 Galaxies and their Place in the Universe, PoS (NLS1), 024
Foschini, L., Berton, M., Caccianiga, A., et al. 2015, A&A, 575, A13
Foschini, L., Lister, M. L., Antón, S., et al. 2021, Universe, 7, 372
Franceschini, A., Vercellone, S., & Fabian, A. C. 1998, MNRAS, 297, 817
Gabányi, K. É., Frey, S., Paragi, Z., et al. 2018, MNRAS, 473, 1554
Giroletti, M., & Polatidis, A. 2009, Astron. Nachr., 330, 193
Goodrich, R. W. 1989, ApJ, 342, 224
Graham, A. W., & Driver, S. P. 2005, PASA, 22, 118
Hamilton, T. S., Berton, M., Antón, S., et al. 2021, MNRAS, 504, 5188
Hardcastle, M. J., Alexander, P., Pooley, G. G., & Riley, J. M. 1998, MNRAS, 296, 445
Hota, A., Sirothia, S. K., Ohyama, Y., et al. 2011, MNRAS, 417, L36
Jarrett, T. H. 2000, Astron. Soc. Pacific, 112, 1008
Järvelä, E., Lähteenmäki, A., Lietzen, H., et al. 2017, A&A, 606, A9
Järvelä, E., Lähteenmäki, A., & Berton, M. 2018, A&A, 619, A69
Järvelä, E., Berton, M., & Crepaldi, L. 2021, Front. Astron. Space Sci., 8, 147
Järvelä, E., Dahale, R., Crepaldi, L., et al. 2022, A&A, 658, A12
Keel, W. C., White, I., R. E., Owen, F. N., & Ledlow, M. J. 2006, AJ, 132, 2233
Kellermann, K. I., Sramek, R., Schmidt, M., Shaffer, D. B., & Green, R. 1989, AJ, 98, 1195
Kharb, P., O'Dea, C. P., Baum, S. A., et al. 2008, ApJS, 174, 74
Klindt, L., Alexander, D. M., Rosario, D. J., Lusso, E., & Fotopoulou, S. 2019, MNRAS, 488, 3109
Komossa, S., Voges, W., Xu, D., et al. 2006, AJ, 132, 531
Kormendy, J., & Gebhardt, K. 2001, in 20th Texas Symposium on Relativistic Astrophysics, eds. J. C. Wheeler, & H. Martel, AIP Conf. Ser., 586, 363
Kotilainen, J. K., Hyvönen, T., & Falomo, R. 2005, A&A, 440, 831
Kotilainen, J. K., León-Tavares, J., Olguín-Iglesias, A., et al. 2016, ApJ, 832, 157
Krongold, Y., Dultzin-Hacyan, D., & Marziani, P. 2001, AJ, 121, 702
Lähteenmäki, A., Järvelä, E., Ramakrishnan, V., et al. 2018, A&A, 614, L1
Magorrian, J., Tremaine, S., Richstone, D., et al. 1998, AJ, 115, 2285
Mao, M. Y., Blanchard, J. M., Owen, F., et al. 2018, MNRAS, 478, L99
Mathur, S., Kuraszkiewicz, J., & Czerny, B. 2001, New Astron., 6, 321
Mathur, S., Fields, D., Peterson, B. M., & Grupe, D. 2012, ApJ, 754, 146
Morganti, R. 2017, Front. Astron. Space Sci., 4, 42
Olguín-Iglesias, A., Kotilainen, J. K., León Tavares, J., Chavushyan, V., & Añorve, C. 2017, MNRAS, 467, 3712

Olguín-Iglesias, A., Kotilainen, J., & Chavushyan, V. 2020, MNRAS, 492, 1450
Orban de Xivry, G., Davies, R., Schartmann, M., et al. 2011, MNRAS, 417, 2721
Osterbrock, D. E., & Pogge, R. W. 1985, ApJ, 297, 166
Padovani, P. 2017, Nat. Astron., 1, 0194
Paliya, V. S., Ajello, M., Rakshit, S., et al. 2018, ApJ, 853, L2
Peng, C. Y., Ho, L. C., Impey, C. D., & Rix, H.-W. 2010, AJ, 139, 2097
Peterson, B. M. 1997, An Introduction to Active Galactic Nuclei (Cambridge: Cambridge University Press)
Peterson, B. M. 2011, in Narrow-Line Seyfert 1 Galaxies and their Place in the Universe, PoS (NLS1), 032
Planck Collaboration XIII. 2016, A&A, 594, A13
Plewa, T., Marti, J. M., Mueller, E., Rozyczka, M., & Sikora, M. 1997, ArXiv e-prints [arXiv:astro-ph/9706124]
Pogge, R. W. 2011, in Narrow-Line Seyfert 1 Galaxies and their Place in the Universe, PoS (NLS1), 002
Rakshit, S., Stalin, C. S., Hota, A., & Konar, C. 2018, ApJ, 869, 173
Rau, U., & Cornwell, T. J. 2011, A&A, 532, A71
Richards, J. L., & Lister, M. L. 2015, ApJ, 800, L8
Salucci, P., Szuszkiewicz, E., Monaco, P., & Danese, L. 2000, MNRAS, 311, 448
Savolainen, T., Wiik, K., Valtaoja, E., et al. 2006, ApJ, 647, 172
Urry, M. 2003, in Active Galactic Nuclei: From Central Engine to Host Galaxy, eds. S. Collin, & F. Combes, ASP Conf. Ser., 290, 3
Urry, C. M., & Padovani, P. 1995, PASP, 107, 803
Vietri, A., Berton, M., Ciroi, S., et al. 2018, in Revisiting Narrow-Line Seyfert 1 Galaxies and their Place in the Universe, PoS (NLS1), 047
Wiegert, T., Irwin, J., Miskolczi, A., et al. 2015, AJ, 150, 81

Appendix A: NIR/optical analysis

A.1. NIR

To perform the photometric decomposition of the Ks-band image, we used GALFIT version 3 (Peng et al. 2010), which allows the simultaneous fitting of several components that contribute to the total 2D light distribution of the source. To properly model the AGN, a good PSF model is needed. GALFIT is capable of extracting the PSF directly from the image of a star once it is centred and sky-subtracted. This allows more accurate PSF modelling since no analytical functions are needed.

We estimated the zero point of the image and its associated error by using stars in the field of view with 2MASS magnitudes in Ks-band and applying the aperture photometry technique. The image was sky-subtracted and the sky error was estimated in several separate regions of 100×100 px. We estimated the sky error effect by fitting with the $\pm 1\sigma$ values. For magnitudes an additional zeropoint estimate error was added.

We modelled the AGN component with a PSF. We tried with several approaches using IRAF as well as different PSF models created in GALFIT. First of all, we used the PSF photometry technique in IRAF. We made several attempts using the *daophot* package. We started by creating a stellar PSF with eleven stars with known 2MASS magnitudes, but more stars were needed to obtain a good PSF. Then, we followed the same procedure as before using multiple stars, but the PSF obtained was still affected by the distortions in the detector along the field of view. To fix this problem, we modelled the PSF shape as a linear function of the position on the image, and we also chose a bigger value for the radius of PSF model (fifteen times the mean FWHM) to see the shape of the stars' wings. This model was still affected by errors due to the field being too crowded. For these reasons, we tried taking the average FWHM of the stars in the image and creating a Gaussian model using GALFIT, and then used it as the PSF model. The PSF size was indeed too small to let the wings be visible. Then, we tried using a nearby star as close as possible to the AGN to minimise the effects of the position-dependent PSF. We extracted the isolated star quite close to the galaxy, and we used this star as the model PSF itself. This attempt was not optimal since the star was quite faint compared to the AGN. We choose to model the nearby star to smooth out any tiny imaging errors affecting the star. We fitted the nearby star with one Gaussian in GALFIT but one function was not enough to properly model the PSF. For this reason, we tried fitting the star in GALFIT with different combinations of Gaussians and exponential discs and extracting the model PSF. The resulting PSF used for the galaxy fit did not give a proper model for the host galaxy. Finally, we obtained the best PSF model fitting five Sérsic functions for the nearby star, freezing the sky mean value to zero in the fit.

The galaxy modelling was started by fitting only the PSF and then adding more components one at a time as required. The residuals were checked after every fit, and the component parameters were varied to ensure the stability of the result. We fixed the central coordinates of the AGN component but kept other parameters free. After achieving a good fit, determined by the reduced χ^2_ν, and after visual inspection of the model and the residuals, we also visually checked all the sub-components to confirm they looked physically reasonable.

The Sérsic profile was used to model the various components of our sources:

$$I(r) = I_e \exp\left[-\kappa_n \left(\left(\frac{r}{r_e} \right)^{1/n} - 1 \right) \right], \tag{A.1}$$

where $I(r)$ is the surface brightness at radius r, and κ_n is a parameter connected to the Sérsic index, n, so I_e is the surface brightness at the half-light radius, r_e (Graham & Driver 2005). By changing the Sérsic index, n, the Sérsic profile can be used to model varying light distributions in galaxies; for example, classical and pseudo-bulges, and early- and late-type morphologies. Smaller values of n ($\lesssim 2$) are associated with galaxies with late-type morphology and pseudo-bulges, and larger values of n ($\gtrsim 4$) with elliptical galaxies and classical bulges (Graham & Driver 2005).

After a good fit was achieved, we extracted the radial surface brightness profile from the observed image, the model image, and the separate component images using the IRAF task *ELLIPSE*, which fits concentric elliptical isophotes to a 2D image. For the original image and the model image, we used similar *ELLIPSE* parameters to get comparable fits. For the individual components, we took the values of the central coordinates, the axial ratio, and the position angle from the GALFIT best-fit parameters. The error estimate takes into account the most important error sources, the sky value error, and the zero point error.